RSC Advances

PAPER

View Article Online
View Journal | View Issue

Check for updates

Cite this: RSC Adv., 2022, 12, 31585

Synthesis of a porous SiO_2–H_3BO_3–V_2O_5–P_2O_5 glassy composite: structural and surface morphological behaviour for CO_2 gas sensing applications†

Zaireen Fatima,[ab] Chandkiram Gautam,*[a] Ajeet Singh,[c] Sarvesh Kumar Avinashi,[a] Bal Chandra Yadav[c] and Afroj Ahmed Khan[b]

Received 19th July 2022
Accepted 19th October 2022

DOI: 10.1039/d2ra04455b

rsc.li/rsc-advances

The present work mainly focuses on the fabrication of a porous glass $40SiO_2$–$35H_3BO_3$–$19V_2O_5$–$6P_2O_5$ *via* a melt-quenching technique. The structural, morphological, and sensing behaviour of the glass sample was investigated successfully. The calculated density and molar volume of the fabricated glass are 2.4813 ± 0.124 g cm^{-3} and 35.7660 ± 1.708 cm^3 mol^{-1}. XRD, SEM and TEM analyses confirmed the amorphous nature of the glass. FTIR results revealed the O–H bond formations, which indicate that the presence of water molecules is probably due to the porous nature of the glass. Further, BET analysis confirmed the mesoporous nature of the glass sample with a mean pore diameter of 7 nm. The sensing response of the synthesized glass at 1000 ppm concentration of CO_2 was found to be 3.05 with a response time 22.6 s and recovery time 25.8 s. Hence, this porous glass can be easily synthesized, is affordable, and was found to be useful for CO_2 gas sensing applications.

Introduction

The demand for better and industrialized surroundings has led to an extreme evolution of harmful gases, and the excessive use of natural resources has resulted in increased air pollution. The need to upgrade and enhance man-made resources for coming generations is increasing day by day, which in turn causes a lot of pollution in the atmosphere.[1] Carbon dioxide (CO_2) is one of the most common toxic gases present in the atmosphere, and the emission from automobiles, greenhouse gases, and industrial plants is the major source of CO_2 emission. The excessive release of CO_2 has a direct impact on the increased temperature, leading to global warming. To control the toxic harmful gases and to prevent the deterioration of the atmosphere, we need to keep pollution levels in check. This led to the discovery of gas sensors that help reduce air pollution by keeping track of harmful gases, such as CO, CO_2, NO_2, methane, in the atmosphere, thus preventing the adverse effects of pollution on all natural beings. The first ever gas sensor was developed in the early 1980s based mainly on household or non-professional purposes such as gas leakage, humidity sensors, and car fuel leakage systems.[2,3] Gradually, the demand for gas sensors increased for various other applications such as air pollutants, volatile organic compounds (VOCs), fire detection, industrial implants, breath analysers, and many more, which led to the advancement of gas sensors in domestic as well as industrial fields.[4–10]

Recently, porous glass has attracted increasing attention due to its unique properties such as porous structure, chemical and thermal stability, and very reactive surface.[11,12] The porous structure of glass provides a large surface area with various active pore sites to adsorb and desorb gas, which elevates the sensing ability of the sensor, thus making it an excellent gas sensor for many applications.[13–15] There is often a discussion as to why only porous materials are considered for gas sensing application over non-porous materials. A non-porous material has a weak sensing response, low selectivity, and requires a high temperature process for the gas sensing mechanism and therefore not suitable for gas sensor applications. Many researchers came forward to present a comparative study of gas sensing properties on porous and non-porous materials having the same composition. Du *et al.* carried out a detailed ethanol gas sensing measurement on porous SnO_2 and non-porous SnO_2 microflowers and revealed that the sensing response for porous SnO_2 (3.05) showed way better results than non-porous SnO_2 (1.5).[16] Song *et al.* synthesized porous ZnO microflowers and non-porous ZnO microflowers by a hydrothermal method and revealed that the response for porous ZnO showed 1.8 times better response results than non-porous ZnO.[17]

Usually, semiconducting metal oxides (SMOs) are preferred for gas sensing. However, it has been revealed in recent research

---

[a] Advanced Glass and Glass Ceramics Research Laboratory, Department of Physics, University of Lucknow, Lucknow, 226007, India. E-mail: gautam_ceramic@yahoo.com

[b] Department of Physics, Integral University, Lucknow, 226026, India

[c] Department of Physics, Babasaheb Bhimrao Ambedkar University, Lucknow, 226025, India

† Electronic supplementary information (ESI) available. See DOI: https://doi.org/10.1039/d2ra04455b

that amorphous materials can also provide excellent gas sensing output due to the availability of large surface area, easy fabrication, and require low temperatures for manufacturing amorphous composites. Many research works have proven that amorphous substances like glass can be used for CO_2 gas sensing applications. Sophia *et al.* demonstrated that when applied voltage and polarisation voltage flow is balanced, a standard soda-lime glass (Sailing Boat Lab, China) can achieve prominent CO_2 gas sensing properties. The sensing response was found to be 0.43 for the highest concentration of CO_2 (5000 ppm).[19] Kumar *et al.* synthesized a multiwalled carbon nanotube (MWCNT) thin film by using the chemical vapor deposition (CVD) technique for CO_2 gas sensing applications. The sensing response for the synthesized MWCNT gas sensor was found to be 2.1 at 5000 ppm of CO_2.[20] Recently, Kim *et al.* investigated the gas sensing properties of pure and Pd-, Pt-, and Au-functionalized soda-lime glasses. The functionalized glasses were prepared *via* the UV-irradiation method for different precursors. The gas sensing results revealed that at a temperature of 350 °C, the gas sensing response for pure soda-lime glass was 1.379 for 5000 ppm concentration of CO_2 gas.[21] More recently, Ali *et al.* synthesized amorphous molybdenum trioxide (MoO_{3-x}) films using the thermal evaporation technique. The MoO_{3-x} thin film deposited on a 650 nm thick glass substrate revealed a relatively high response and recovery time, and the sensor response at 200 °C was recorded to be 2.826.[22] Various amorphous and porous materials have been analysed for CO_2 gas sensing applications. However, not much research has been done on porous glass, which can emerge as a potential contender for gas sensors due to its unique porous morphology and amorphous nature. This study revealed that the synthesized glass showed way better sensing results than many crystalline materials, thus opening a new field for glass applications.

Various metal oxides are being used for glass synthesis, like SiO_2, H_3BO_3, V_2O_5, *etc.* Silicon dioxide (SiO_2) is the main constituent for glass fabrication, and it is widely used as a glass former. SiO_2 basically enhances the electrical, dielectric, and thermal properties of the synthesized glass. Boric acid (H_3BO_3) is commonly used as a fluxing agent for glass preparation. Some oxides used in the glass preparation have relatively high melting temperatures, *e.g.*, SiO_2 (melting temperature ~1713 °C); thus, the inclusion of H_3BO_3 in such oxide glass compositions allows the glass to melt at a lower temperature. Phosphorus pentoxide (P_2O_5) is an extensively used material for glass fabrication because it has unique properties like low melting point and high thermal and chemical stability, making it an efficient sensing material. Besides these oxides, vanadium pentoxide (V_2O_5) has attained a lot of attention in the field of sensor technology due to its high stability and chemical resistance and offers low-cost fabrication for sensors.[3,23–25]

Herein, our main focus is to synthesize a glass $40SiO_2$–$35H_3BO_3$–$19V_2O_5$–$6P_2O_5$ (SHVP6) *via* the melt-quenching technique, which is commonly used for glass preparation and is quite affordable and easy to operate. The structural and morphological properties of this synthesized glass are analyzed in detail. We know that the porous structure helps in elevating the sensing ability of the gas sensor. Therefore, the porous morphology of the synthesized glass indicated the possible gas sensing application. Hence, this porous glass is subjected to carbon dioxide (CO_2) gas sensing, and a detailed gas sensing analysis is performed to study different parameters like sensor response, response time, and selectivity of porous glass SHVP6.

Experimental

Fabrication of glass sample

Melt-quenching technique (MQT) is widely used for glass preparation. High quality chemical reagents used to fabricate $40SiO_2$–$35H_3BO_3$–$19V_2O_5$–$6P_2O_5$ glass were SiO_2 (Himedia 99.5%), H_3BO_3 (Himedia 99.5%), V_2O_5 (Sigma-Aldrich 98%), and P_2O_5 (Sigma-Aldrich 98%). Appropriate amounts of given chemicals were weighed in an electronic balance, and a batch of 25 g was mixed together with the help of a mortar and pestle with acetone as a mixing medium for 2 h. This mixture was then poured into an alumina crucible and kept in a programmable furnace at 1400 °C with a heating rate of 5 °C min^{-1}. The prepared melt was left in the furnace for an additional 30 min (soaking time) so as to properly homogenize. This melt was then taken out from the furnace and was poured onto an aluminium mould and immediately quenched with the help of an aluminium plate for residual stress removal within the fabricated glass. The sample was then kept in a pre-heated muffle furnace at 400 °C with a heating rate of 5 °C min^{-1} for 4 h. The fabricated glass samples were taken out of the furnace after cooling to room temperature. The prepared glass was taken out when the furnace was cooled to room temperature (30 °C).[7,26] The schematic diagram for glass preparation is shown in Fig. 1(a).

Device fabrication and CO_2 sensor fabrication

To prepare a thin film of porous glass sample, the method employed was as follows: a homogeneous solution was prepared by dissolving the synthesized SHVP6 porous glass in hydrofluoric acid (HF); the solution was prepared using ultra-sonification. This solution was then drop-coated on a glass substrate of dimensions 1 × 1 cm^2 and dried at 70 °C on a hot plate. A specially designed gas chamber was used to analyse the characteristics of CO_2 gas sensing. The sensing film was mounted on the sample holder, and silver electrodes were connected to the surface of the sensing film and dried at 60 °C. The inlet of the gas chamber is connected to a measuring unit: CO_2 regulator, which is used to measure the accurate concentration of the CO_2 gas that flows inside the chamber. The leads from the outer end of the gas chamber were connected to the Keithley electrometer 6517B for estimating the electrical resistance of the gas sensing film. A schematic diagram for the gas sensing setup is shown in Fig. 1(b), and the gas sensing measurement was carried out at room temperature (32 °C and 60% RH).[27]

XRD of the porous glass sample

The synthesized samples were ground for 1.5 h to make a fine powder. To analyze the amorphous nature of the synthesized samples, the XRD pattern of this powdered sample was recorded within a 2θ range of 10°–70° with scanning @ 5° min^{-1}

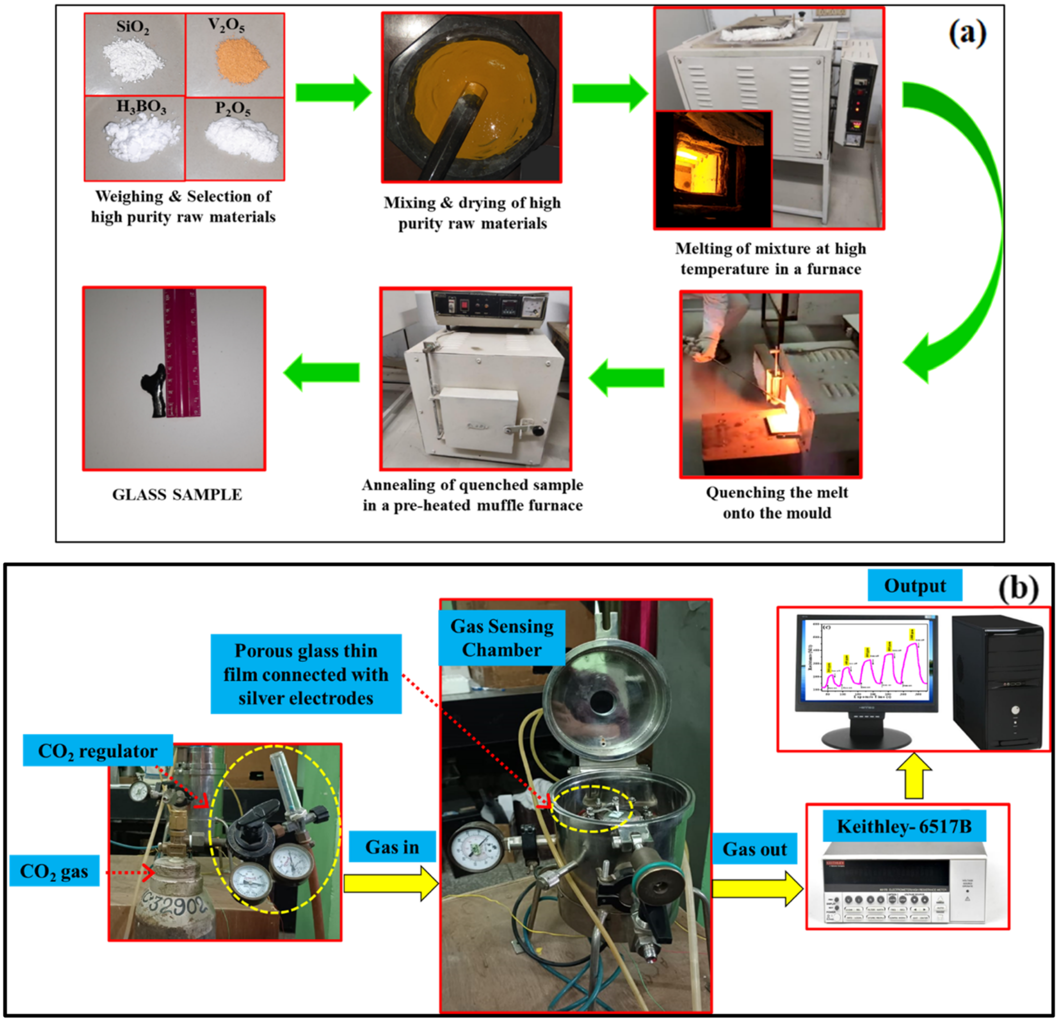

Fig. 1 (a) Schematic diagram for the fabrication of glass sample *via* the melt-quenching technique, (b) schematic diagram of CO_2 gas sensing setup.

using a Rigaku Ultima IV XRD machine having a monochromatic CuKα radiation ($\lambda = 1.54$ Å) that functioned at 40 kV and tube current at 40 mA.

Density and molar volume

The density of the porous glass was calculated with the help of Archimedes' principle. Irregular shaped glass samples were used to analyse the density of the synthesized porous glass. The measurement was performed with the help of an electronic balance having readability up to 0.0001 mg, and distilled water was used as a liquid medium. To obtain accurate results, the density measurement was repeated three times, and the average value was taken into consideration. The density of the synthesized porous glass was calculated by using the formula given below:[7]

$$\rho = \frac{(W_2 - W_1)}{(W_4 - W_1) - (W_3 - W_2)} \times \rho_W \quad (1)$$

where, ρ_W is the density of distilled water ($\rho_W = 1$), W_1 is the weight of an empty density bottle, W_2 is the weight of a density bottle with a porous glass sample, W_3 is the weight of density bottle with distilled water and porous glass sample, and W_4 is the weight of the density bottle with distilled water. On the other hand, the molar volume (V_m) of the porous glass sample was calculated using the formula given in eqn (2)

$$V_m \ (\text{cm}^3 \ \text{mol}^{-1}) = \frac{M \ (\text{g mol}^{-1})}{\rho \ (\text{g cm}^{-3})} \quad (2)$$

where V_m represents the molar volume of the porous glass sample, M represents the molar mass, and ρ is the density of the porous glass sample.[7]

Brunauer–Emmett–Teller (BET) measurements

To analyse the surface area, pore size, and surface porosity of a powdered porous glass sample, BET is performed. This analysis reveals the significant properties and importance of the sample in the field of sensor technology. Micrometrics (Gemini VII 2390t) surface area analyser at an adsorption temperature of 77 K was used to determine the pore size, surface area, and porosity of the porous glass sample.

FT-IR and Raman spectroscopy measurements

FT-IR spectroscopy is used to study the structural information of the synthesized sample. To analyse and record the FTIR spectra of the synthesized porous glass, a fine powder of SHVP6 glass and KBr (Potassium bromide) is mixed with the help of a mortar and pestle to make a fine powder and then pressed to form a thin circular pellet using a hydraulic press machine. These thin pellets were used to record the FTIR spectrum through an IRAffinity-IS FTIR (SHIMADZU-01020) within the wavenumber range of 400 to 4000 cm^{-1}. Further, the recorded spectra of the SHVP6 porous glass displayed numerous transmittance bands in different wavenumber regions. Raman spectra were recorded using a MicroRaman setup (Renishaw, UK) that was furnished with 1800 lines per mm diffraction grating within the wavenumber range of 0–1200 cm^{-1}.

Scanning and transmission electron microscopy

To study the surface morphology of the synthesized glass sample, SEM was performed. The surface of the glass sample was polished using different silicon carbide (SiC) powders (mesh number: 120, 600, and 800) to obtain a plain surface. The porous glass was further polished using emery paper (grade 2000, 2500, 3000, and 3500) and then rubbed on a soft blazer cloth using a diamond paste of particle size 1–6 μm along with Hifin fluid 'OS'. The polished glass sample was then washed with double distilled water to remove any debris from the surface and then placed in an electric oven for 1 h to dry. To avoid any charge accumulation, a sputtering unit is used, Auto Fine Coater JEOL (Model: JEC-3000FC) is used to spread thin gold films on the surface of the glass sample. The polished sample was mounted on a copper stub with the help of a carbon tape, and SEM images were recorded at different magnifications with the help of SEM-Model: JSM-7610 F, Make: JEOL Ltd Japan.[26] The TEM images and diffraction patterns were recorded with the help of TEM (JEOL, Model: JEM 2100). A small quantity of finely powdered sample was taken and kept in an isopropyl alcohol bath for about 30 min. The sample for TEM analysis was prepared by casting a few drops of sample on the grid and left to dry in a vacuum overnight.[28]

Energy dispersive spectroscopy (EDS) measurements

To evaluate the elemental constituents present in the synthesized porous glass, EDS was performed. This technique is quite useful in quantitative as well as qualitative studies. In this technique, a selected area/spot of the porous glass was scanned, and the presence of elements was examined and recorded. Thus, the EDS spectrum reveals the desired elemental information about the synthesized porous glass sample.[26]

Results and discussion

Density and molar volume of the porous glass

The density and molar volume of the prepared glass sample are 2.4813 ± 0.124 g cm^{-3} and 35.7660 ± 1.708 cm^3 mol^{-1}, respectively. The density of the synthesized glass SHVP6 is found to be less than the standard density of SiO_2 (2.65 g cm^{-3}) and the density of V_2O_5 (3.36 g cm^{-3}). The density of the glass sample was calculated using the Archimedes principle. The decrease in the density of the prepared glass is probably due to the presence of voids/holes in the structural arrangement of the SHVP6 glass, thus indicating the porous nature of SHVP6 glass.[7]

X-ray diffraction analysis

The XRD analysis of the synthesized glass $40SiO_2$–$35H_3BO_3$–$19V_2O_5$–$6P_2O_5$ is shown in Fig. 2. The XRD analysis shows diffused peaks with short-range order, confirming the amorphous nature of the prepared glass.[26] The absence of sharp peaks depicts that the prepared sample has no major phase formation or grain boundaries, which is further confirmed by the TEM characterization discussed later in this paper.

Fourier transform infra-red spectroscopy

A FTIR spectrum for the synthesized glass SHVP6 is shown in Fig. 3(a), and a series of transmittance peaks have been observed in the range of 400–4000 cm^{-1}. Multiple peaks have been observed in the low wavenumber region (fingerprint region), and the low intensity peak at 443 cm^{-1} corresponds to the Si–O rocking vibration, indicating the presence of SiO_2 within the glass sample. Another low intensity transmittance peak at 547 cm^{-1} corresponds to the vibration of the V–O bond. Also, a weak intensity transmittance peak at 650 cm^{-1} is assigned to the wagging vibrations of Si–H bonding. The low wavenumber region is mainly comprised of silicate bonds, and this might be due to the highest content of SiO_2 present in the glass composition.[29–31] Another low intensity peak at 1195 cm^{-1} shows the asymmetric stretching vibration of PO_2.[32] A broad peak at 1456 cm^{-1} is observed, which indicates the characteristics of –O– vibrations.[33] Peaks at 1622 cm^{-1}, 2926 cm^{-1}, and 3215 cm^{-1} are assigned to the stretching vibration of O–H bonds inside the porous glassy network. The presence of O–H bonding is probably due to the porous nature of the synthesized glass and also due to the high hygroscopicity of P_2O_5.[34,35,37]

Raman spectroscopy

Fig. 3(b), shows the Raman spectrum of the synthesized porous glass, weak intensity peaks at 187 cm^{-1}, 498 cm^{-1}, and 684 cm^{-1} correspond to the bending vibration of O–Si–O bond, Si–Si vibration, and symmetric stretching vibration of Si–O–Si,

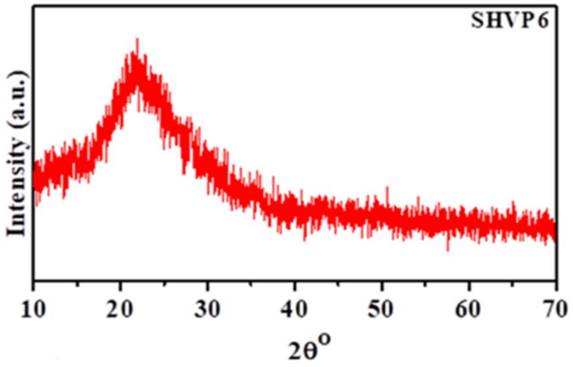

Fig. 2 XRD pattern of porous glass sample SHVP6.

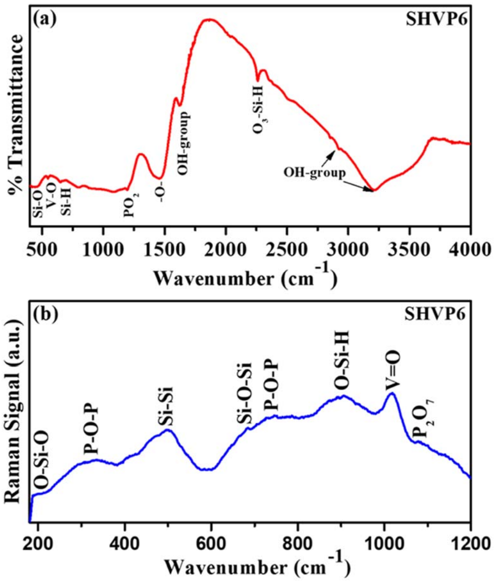

Fig. 3 (a) FTIR spectrum of the SHVP6 porous glass, (b) Raman spectrum of the SHVP6 porous glass.

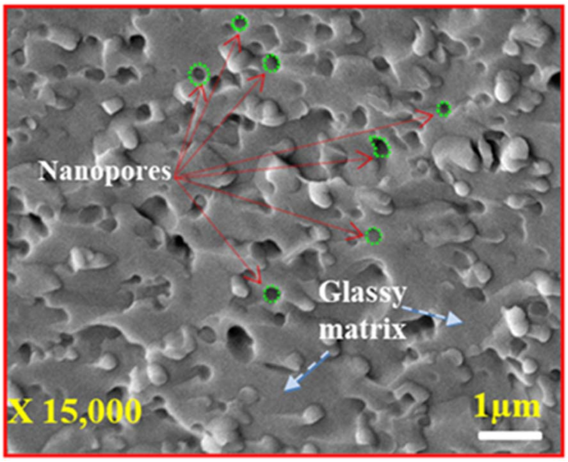

Fig. 4 High-magnification SEM micrograph of glass sample.

respectively. These peaks indicate the presence of SiO_2 within the glassy matrix, which is in good agreement with the.

FTIR spectroscopic analysis.[38,40] The weak intensity peaks at 336 cm^{-1} correspond to vibrations of the pyrophosphate group through a P–O–P linkage.[39] A sharp peak is observed at 1018 cm^{-1}, indicating the vibration of V═O; this strong vibration peak indicates that these vanadium species also interact with water molecules to form hydrated species of V_2O_5, and this reaction is probably due to the porous nature of the synthesized glass sample, which is discussed later in this paper.[43] The detailed peaks and their respective vibrational bonding of FTIR and Raman spectra are shown in Table 1.[29–44]

Scanning electron microscopy and elemental analysis

Fig. 4 shows a high magnification SEM image of the synthesized glass, and the image clearly shows distinct spherical pores having varied pore sizes randomly spread across the surface of the glass sample (indicated by green circles). The average pore diameter of these pores ranges from 0.167–0.322 µm, which are embedded on the glassy matrix as shown in Fig. 4 (indicated by blue dotted lines). Since the pore diameter varied significantly, we can only indicate that the synthesized glass is porous in nature; therefore, TEM microscopy will be discussed later in this paper to analyse the porous as well as amorphous nature of the fabricated glass in a more detailed manner. This pore formation is possibly due to the high temperature manufacturing of the glass, which is synthesized at a temperature of 1400 °C. At high temperatures, the boric acid (H_3BO_3) present in the glass decomposes as shown in eqn (3):

$$H_3BO_3(s) \xrightarrow{\Delta} HBO_2(g) + H_2O\uparrow \tag{3}$$

The reaction gives out metaboric acid (HBO_2) along with the release of water molecules from the glass melt,[45,46] thus generating pores on the surface of the glass sample.

Further, there is no visible grain or grain boundary, thus confirming the amorphous nature of the glass, which is in good agreement with the XRD results.

Further, the elemental mapping was performed on a low magnification SEM image, as shown in Fig. S1(a),† to study the distribution of elements on the surface of the prepared glass sample. Fig. 5(a) shows the average distribution of elements on the surface of the glass, the distribution of elemental composition of this homogeneous mixture is further shown in

Table 1 Peak assignment for FTIR and Raman spectra with their respective wave number

FTIR wavenumber (cm^{-1})	Vibration type	References	Raman wavenumber (cm^{-1})	Vibration type	References
443	Si–O rocking vibration	29	187	O–Si–O bending vibration	38
547	V–O vibration	30	336	PO_3 deformation vibration	39
650	SiO_4 bending vibration	31	498	Si–Si vibration	40
1195	PO_2 asymmetric stretching vibration	32	684	Si–O–Si symmetric stretching	38
1456	–O– vibration	33	745	P–O–P symmetric stretching	41
1622, 2926	O–H group	26, 34 and 35	905	O–Si–H bending/P–O–P asymmetric stretching vibration	38 and 42
2260	O_3–Si–H stretching vibration	36	1018	V═O vibration	43
3215	O–H group	37	1078	P–O symmetric stretching vibration	44

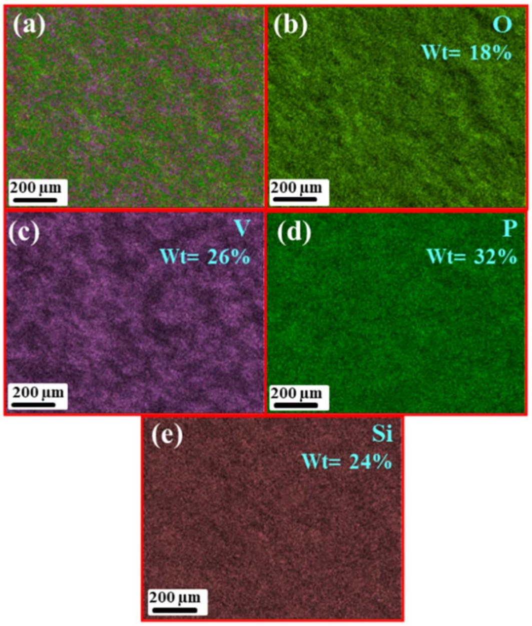

Fig. 5 (a) Average elemental mapping of porous glass, SEM-EDS elemental mapping: (b) O-18%, (c) V-26%, (d) P-32%, (e) Si-24%.

Fig. 5(b)–(e) where 18% of oxygen (indicated by light green color), 26% of vanadium (indicated by purple color), 32% of phosphorus (indicated by dark green color), and 24% of silicon (indicated by light beige color), respectively. The mapping results reveal that phosphorus and vanadium have major contributions to the glass formation. The pie chart (Fig. S1(b)†) shows the elemental distribution of components in the synthesized glass.

Energy dispersive spectroscopy (EDS) is performed to determine the elemental distribution of elements present on the surface of the porous glass (Fig. 6). The EDS spectrum of the synthesized glass further confirmed the presence of elemental composition (average) of silicon (Si), oxygen (O), vanadium (V), and phosphorus (P) along with some impurities like aluminium (Al). The impurity (Al) present in the synthesized glass sample was probably due to the use of aluminium crucible for the high temperature melting process. The weight percentage of vanadium (V) is 32.56%, phosphorus (P) is 15.71%, silicon (Si) is 9.04%, and aluminium (Al) is 0.73%. The graph suggests that the weight percentage of oxygen (O) is 41.96% due to the contribution of oxides in the preparation of the glass sample[26]

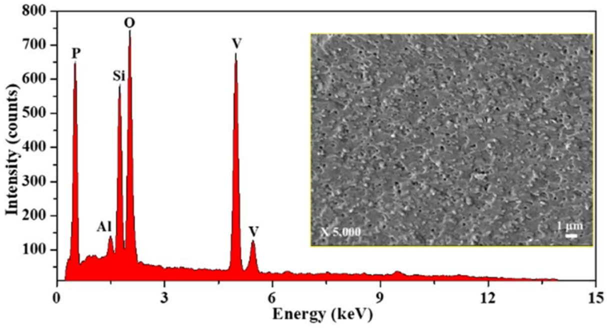

Fig. 6 EDS spectrum of the porous glass sample SHVP6.

Transmission electron microscopy

Since the SEM micrograph records the morphology of the sample surface, TEM analysis is performed to study the morphology of the glass sample more closely. Fig. 7(a) shows the TEM image of SHVP6 glass, the overlapped spherical pores spread across the glass sample indicate that the fabricated glass has porous morphology, and these pores have an average pore diameter of 33.42 nm, which is in good agreement with the SEM results.

The TEM image of SHVP6 glass is shown in Fig. 7(b), and petal-like dark region can be seen in the high-resolution TEM image, which shows a magnified pore. The TEM image reveals the presence of petal-like dark regions; these darker regions (petal-like structure) probably correspond to V-rich zones owing to their high density (6.11 g cm^{-3}), while the lighter regions correspond to (Si, P, O, H) rich zones.[47]

The inset in Fig. 7(b) shows a selected area electron diffraction (SAED) pattern, and the SAED pattern clearly depicts the diffused rings confirming the amorphous nature of the porous glass.[48] Fig. 7(c) shows an HR-TEM image, and no lattice fringe or grain boundaries were observed, which confirms that the fabricated glass is amorphous in nature. These results are consistent with the XRD as well as SEM analysis, which also confirm the amorphous nature of the synthesized porous glass.

Brunauer–Emmett–Teller (BET) analysis

The SEM and TEM analyses indicate the porous morphology of the fabricated glass, and therefore, BET and BJH analysis was performed to confirm the porous nature of the synthesized glass SHVP6. To calculate the specific surface area of the porous sample *via* physical adsorption technique of gas molecules on the surface of the porous sample, Brunauer–Emmett–Teller (BET) analysis was performed. The total surface area S_{total} and the specific surface area S_{BET} are given by

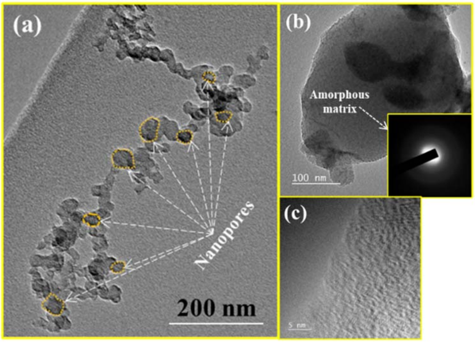

Fig. 7 TEM micrographs of the glass sample: (a) overlapped spherical pores of average pore diameter 33.42 nm, (b) TEM micrograph and SAED-pattern (inset) and (c) and HR-TEM-image of SHVP6 porous glass.

$$S_{\mathrm{t}} = \frac{v_{\mathrm{m}} N S}{V} \tag{4}$$

where, S_{t} is the total surface area of the sample, v_{m} is the monolayer absorbed gas volume, N is the Avogadro's number (6.02×10^{23} molecules per mol), S is the cross-sectional area of adsorbed gas molecule, V is the molar volume of the adsorbed gas

$$S_{\mathrm{BET}} = \frac{S_{\mathrm{total}}}{a} \tag{5}$$

S_{BET} is the specific area, and 'a' is the mass of the sample.

The calculated surface area of the synthesized glass is 70.8 $\mathrm{m^2\ g^{-1}}$, and the large surface area also indicates the amorphous nature of the sample.[11,49] The total pore volume and mean pore diameter of the SHVP6 glass is found to be 0.1288 $\mathrm{cm^3\ g^{-1}}$ and 7.2799 nm, respectively. The nitrogen adsorption–desorption curve of the SHVP6 glass is shown in Fig. 8(a), and the graph indicates Type-IV isotherm, which further reveals that the synthesized glass is porous in nature. The mean pore diameter reveals a lot of information about the pores present; if the mean pore diameter is greater than 50 nm, then the sample has macroporous nature, if the mean pore diameter lies between 2–50 nm then the sample has mesoporous nature, and if the mean pore diameter is less than 2 nm then the sample has microporous nature. The synthesized SHVP6 glass has a mean pore diameter of 7 nm, which lies within the range of 2–50 nm, thus confirming that the fabricated porous glass is mesoporous in nature and is in good agreement with SEM and TEM results.[50] The BJH (Barrett–Joyner–Halenda) plot is used to measure the pore-size distribution of the synthesized glass sample. The average pore diameter of the SHVP6 glass is 1.66 nm, as shown in Fig. 8(b), which confirms the presence of pores within the glassy matrix. Since the prepared glass is mesoporous in nature, the mesoporous surface area (a_{P}) and mesoporous volume (V_{P}) are 65.666 $\mathrm{m^2\ g^{-1}}$ and 0.1224 $\mathrm{cm^3\ g^{-1}}$, respectively.[51] These results are in good agreement with each other and the porous nature of the synthesized glass provides a possible pathway for the target gas, which indicates that the fabricated glass can be used for gas sensing applications. Therefore, gas sensing was performed to analyse various parameters in detail.

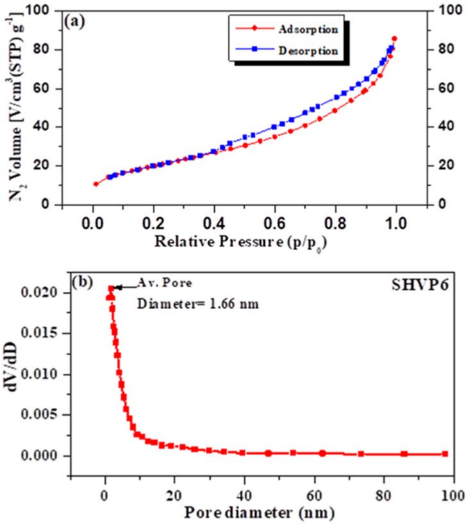

Fig. 8 (a) Nitrogen adsorption–desorption curve of porous glass sample SHVP6. (b) Pore size distribution of the glass sample by BJH method.

Gas sensing properties of porous glass

The $\mathrm{CO_2}$ gas sensor works on the phenomena of adsorption (ads) and desorption. The variation in electrical resistance of the sensing film occurred due to the adsorption/desorption of $\mathrm{CO_2}$ gas on the sensing surface. The parameters taken into consideration to study the sensing properties of $\mathrm{CO_2}$ gas for SHVP6 porous glass are sensing response, response time, and recovery time with a concentration range of 200–1000 ppm (parts per million) at room temperature. The $\mathrm{CO_2}$ sensing graphs recorded at different concentrations of 200, 400, 600, 800, and 1000 ppm with exposure time are shown in Fig. 9(a), and it can be observed that at 200 ppm concentration, the resistance in air (R_{a}) is 115.919 MΩ and the resistance of the glass film suddenly increases when exposed to $\mathrm{CO_2}$ gas inside the chamber and becomes constant at 214.115 MΩ. Afterwards, $\mathrm{CO_2}$ gas is released by opening the outlet of the gas chamber. Other $\mathrm{CO_2}$ gas concentrations were recorded in a similar manner, and the respective curves were plotted.

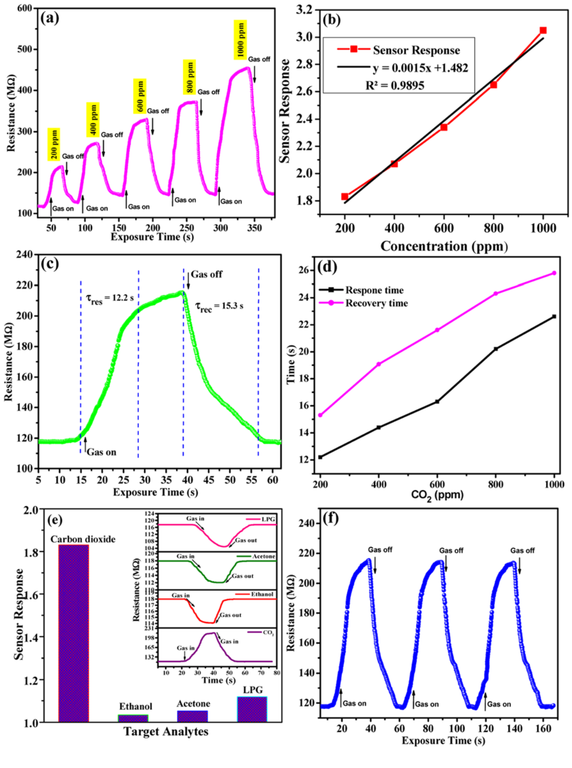

Fig. 9 $\mathrm{CO_2}$ gas sensing characteristics of porous glass, (a) $\mathrm{CO_2}$ sensing curves for different concentrations, (b) sensor response curve with various concentration of $\mathrm{CO_2}$, (c) transit sensor response curve for 200 ppm of $\mathrm{CO_2}$, (d) response and recovery time graphs with different concentrations, (e) selectivity graph at 200 ppm of gas analysts, (f) repeatability graph at 200 ppm of $\mathrm{CO_2}$.

The sensing response of the gas sensor is defined as:

$$\mathrm{SR} = \frac{R_g}{R_a} \tag{6}$$

where, R_a is the resistance in air and R_g is the resistance of the glass film in the presence of CO_2 gas.

The sensing response of glass film for different concentrations of CO_2 (200–1000 ppm) is calculated using eqn (8) and plotted in Fig. 9(b). As the concentration of CO_2 increases, the sensing response increases, as indicated by the linear curve. With the help of this calibrated linear curve (linear fit curve), the sensitivity of the sensing device can be calculated by the IUPAC definition (sensitivity = sensor response/concentration). The sensitivity of the sensing device was found as 0.0091 sensor response/ppm. It is observed that the interaction between the adsorbed oxygen species and CO_2 molecules deteriorates at low concentrations. On increasing the concentration of CO_2 inside the gas chamber, the molecules are adsorbed by the porous film of SHVP6 glass, thus increasing the resistance of the film. The minimum sensor response of the SHVP6 porous glass is found to be 1.83 for 200 ppm of CO_2 and the maximum sensor response is 3.05 for 1000 ppm of CO_2 as shown in Table S2.† The response time (T_{res}) is defined as the time required by the sensor to attain maximum resistance when gas is exposed inside the chamber, whereas the time required by the sensor to come back to its initial state when gas is removed from the gas chamber is the recovery time (T_{rec}). The sensor response, response time, and recovery time were calculated by the transits sensor response graph for porous glass SHVP6 film for various concentrations of CO_2 gas.[52] The transits response graph at 200 ppm concentration of CO_2 is shown in Fig. 9(c), and the response time and recovery time are found to be 12.2 s and 15.3 s, respectively. Similarly, for other concentrations of CO_2 at 400, 600, 800, and 1000 ppm, response and recovery time are calculated as shown in Fig. 9(d). To further check the selectivity of the SHVP6 sensing film with respect to other target analytes like acetone, ethanol, and LPG, comparative data against sensing response is shown in Fig. 9(e). Here, the sensing responses for acetone, ethanol, LPG, and CO_2 are 0.32, 0.53, 0.98, and 1.83, respectively, at 200 ppm concentration. Also, the selectivity curve for various target analytes is shown in Fig. 9(e) (inset). The curve shows that the resistance increases in the case of CO_2 gas, while in the case of other target analytes, the resistance decreases. This analysis further confirms the oxidising nature of CO_2 gas and that the synthesized sample is an n-type material. The sensing response of CO_2 with respect to the other target analytes is relatively higher. The ability to produce the same output after an interval of time for the same parameters is known as the reproducibility of the gas sensor. The repeatability of the sensor is a key parameter, and it can be defined as the same output over one measurement. The repeatability curve at 1000 ppm of sensing film is shown by three consecutive cycles, and it is observed that the measurement is almost 98% repeatable (Fig. 10(a)). Also, the long-term stability of a sensor is a vital parameter and is defined as the ability to reproduce the same measurement after a time interval. The long-term stability curve of SHVP6 sensing film was examined after 15 days' time interval at 1000 ppm, as shown in Fig. 10(b). The sensor response of the sensing curve is calculated using eqn (8) and plotted in Fig. 10(c). As the number of days increases, the sensor response decreases because the presence of moisture weakens the interaction of the CO_2 sensing film. The error bar in the sensor response is shown in Fig. 10(c) and suggests minor changes in sensor response.

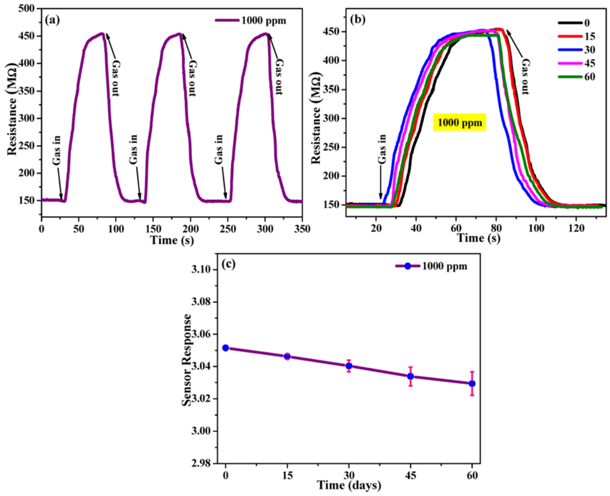

Fig. 10 (a) Sensing characteristics at 1000 ppm of CO_2 showing, (b) long-term stability curve at 1000 ppm and (c) sensor response graph at 1000 ppm of CO_2.

To analyse the gas sensing in detail, various parameters have been calculated, *viz.*, sensitivity, the limit of quantification (LOQ), and the limit of detection (LOD). The sensitivity of the SHVP6 porous glass was calculated using the linear-square fit method and straight-line formula; $y = mx + c$, where y is the sensitivity of the sensing device, m is the response, and c is the CO_2 gas concentration. The correlation plot between CO_2 gas concentration and sensing response of the SHVP6 porous glass is shown in Fig. 9(b), which indicates $y = 0.0015x + 1.482$ and $R^2 = 0.9895$, which reveals the fabricated SHVP6 porous glass is 98% sensitive. The limit of detection is defined as the lowest amount of analyte in the synthesized sample, which can be detected but not necessarily quantified under specified conditions. However, the limit of quantification is the lowest concentration of an analyte in the synthesized sample that can be quantitatively determined with acceptable precision and accuracy under specified conditions. The LOD and LOQ values were calculated using the following equations;

$$\text{Limit of detection (LOD)} = \frac{3.3 \times \mathrm{SD}}{m} \tag{7}$$

$$\text{Limit of quantification (LOQ)} = \frac{10 \times \mathrm{SD}}{m} \tag{8}$$

where SD is the standard deviation of response. The calculated values of LOD and LOQ were found to be 292 ppm and 886 ppm, respectively. These results reveal that the synthesized porous glass sensor is quite stable with excellent CO_2 gas sensing properties.[23,53]

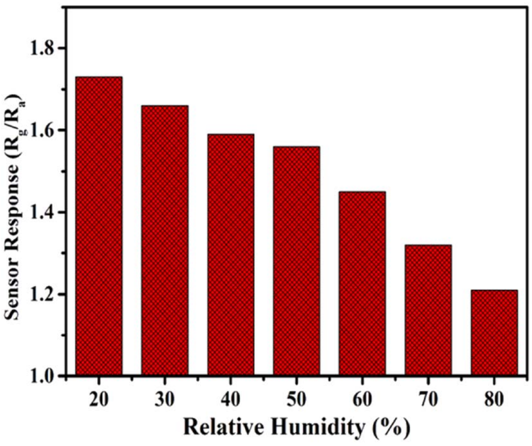

Fig. 11 Relative humidity graph of CO_2 gas sensor.

We also performed the effect of humidity in the presence of CO_2 gas at 200 ppm. Humidity inside the gas chamber was measured with the help of a hygrometer placed inside the gas chamber, and the humidity increased gradually from 20% to 80%, and their respective sensor response was recorded. Fig. 11 shows the sensing response curve of a porous glass film in the presence of relative humidity. Relative humidity present inside this gas chamber was controlled with the help of potassium sulfate (K_2SO_4) solution, which acts as a humidifier. Hence, we conclude that porous glass film shows a decrease in the sensing response when humidity increases. This decrease in sensing response might be due to the increased amount of water molecules in the synthesized sample when humidity is increased. A comparative study of CO_2 gas at different concentrations with respect to previously reported literature is tabulated in Table 2.[20,22–25,54–57]

Gas sensing mechanism

The gas sensing mechanism of metal oxides is explained by the adsorption/desorption surface phenomena. Usually, the electrical resistance increases or decreases depending on the nature of the material (n-type or p-type). Generally, the electrical resistance in n-type semiconductors increases after the interaction of oxidizing gases, whereas the resistance is the opposite for reducing gases. Since the CO_2 gas is oxidizing in nature and it interacts with n-type materials, the resistance should increase. The oxygen present in air gets adsorbed on the surface of the porous glass film even before exposure to CO_2 gas, and the trapped electrons from the conduction band (CB) result in the formation of oxygen species such as O_2^-, O^-, and O^{2-}, which depends upon temperature. The possible reactions can be explained as follows:

$$O_{2(gas)} \rightarrow O_{2(ads)} \tag{9}$$

$$O_{2(gas)} + e^-(CB) \rightarrow O^-_{2(ads)}\ (>100\ ^\circ C) \tag{10}$$

$$O^-_{2(ads)} + e^-(CB) \rightarrow 2O^-_{(ads)}\ (200\text{–}300\ ^\circ C) \tag{11}$$

$$2O^-_{(ads)} + 2e^-(CB) \rightarrow 2O^{2-}_{(ads)}\ (<300\ ^\circ C) \tag{12}$$

At room temperature, O_2^- is formed at the surface of the sensing film and creates an electronic depletion layer, which eventually forms a region known as the depletion region and this depletion region acts as a potential barrier. When the resistance of the porous glass sensing film increases and reaches a saturation point, the adsorption resistance of the porous glass reaches a constant value. When the CO_2 gas reacts with these oxygen species, due to the oxidizing nature of CO_2, the electrons are transferred to CO_2 molecules and form metastable (CO_3^{2-}) complexes on the surface of the sensing film. The formation of (CO_3^{2-}) complexes results in the reduction of the

Table 2 Comparative study of CO_2 gas sensor: materials, synthesis process, CO_2 concentrations, operating temperature, response and recovery time, sensor response

Materials	Synthesis process	Concentration (ppm)	Temperature (°C)	Response time (s)	Recovery time (s)	Sensor response	References
Al_2O_3–V_2O_5	Co-precipitation	600	673	—	—	1.00	20
Standard soda-lime glass	—	5000	350	—	—	0.43	22
MWCNT	DLICVD*	5000	30	30.2	49.6	2.1	23
Pure soda-lime glass	—	5000	350	—	—	1.379	24
MoO_{3-x} thin film	Thermal evaporation	—	200	~180	~180	2.826	25
Ag–$BaTiO_3$–CuO	Thin film deposition	5000	250	900	600	1.28	54
Al/ZnO	Screen printing	1000	250	25	110	2.873	55
Random CNT	CVD	500	RT	385	421	2.19	56
Aligned CNT	CVD	500	RT	33	46	2.08	56
$NdFeO_3$	Sol–gel	1000	200	407	100	1.39	57
SHVP6	MQT	200	RT	12.2	15.3	1.83	Present work
SHVP6	MQT	1000	RT	22.6	25.8	3.05	Present work

conductivity of the sensing film, which increases the depletion region. Hence, there is a sudden increase in the resistance, which depends upon the concentration of CO_2. The possible reactions are as follows:

$$2CO_2 + O_{2(ads)}- + 3e^- \rightarrow 2{CO_{3(ads)}}^{2-} \quad (13)$$

$$2{CO_{3(ads)}}^{2-} \rightarrow CO_2 + 3e^- \quad (14)$$

when the flow of CO_2 is turned off, the $({CO_3}^{2-})$ complexes become CO_2 and the electrons are released from the sensing film, which comes back to its initial state. In the present work, we have observed an enhanced sensing response due to the unique porous morphology, which forms a reactive surface for CO_2 detection, and the mesopores present within this amorphous glassy composite provide a large surface area for CO_2 gas sensing[18].

Conclusion

In this study, a porous glass $40SiO_2–35H_3BO_3–19V_2O_5–6P_2O_5$ was prepared using the melt-quenching technique. X-ray diffraction confirmed the amorphous nature of the glass. SEM and TEM analysis confirmed that the synthesized glass has amorphous nature and revealed the presence of pores within the glassy matrix. BET analysis further confirmed that the pores generated within the fabricated glass are mesoporous, having a mean pore diameter of 7 nm. The porous structure of the glass sample tends to elevate the reactive surface, which increases the sensing response of the CO_2 gas. The sensing response of the porous glass was found to be 3.05 at 1000 ppm of CO_2 gas. Thus, we can say that the unique morphology of this glass provides good sensing ability and opens new ways to fabricate a better gas sensor using porous-amorphous materials with a relatively large surface area using an easy and low-cost fabrication process.

Author contributions

The manuscript was written with the joint contribution of ZF, CRG, and AS under the supervision of CRG. Synthesis, spectroscopic experiments, and sample analysis were performed by ZF and SKA. Sensing experiments were performed by AS and BCY, and the basic calculations were analyzed and calculated by ZF, AS, and AAK. The manuscript was reviewed and approved by all the authors. CRG and AS came up with the idea and topic of the manuscript.

Conflicts of interest

There are no conflicts to declare.

Acknowledgements

The authors are thankful to the Head, Department of Chemistry, University of Lucknow, for extending the FTIR facility and also to Prof. Atul Khanna for providing the Raman measurements at the Department of Physics, Guru Nana Dev University, Amritsar, Punjab India. The Manuscript communication number (IU/R & D/2022-MCN0001619) is allotted from Integral University, Lucknow.

Notes and references

1 Z. Yunusa, M. N. Hamidon, A. Kaiser and Z. Awang, *Sens. Trans.*, 2014, **168**(4), 61–75.
2 N. Yamazoe, *Sens. Actuators, B*, 2005, **108**, 2–14.
3 N. Yamazoe and K. Shimanoe, *Sens. Actuators, B*, 2009, **138**, 100–107.
4 A. Singh, S. Sikarwar, A. Verma and B. C. Yadav, *Sens. Actuators, A*, 2021, **332**, 11312.
5 S. Deng, X. Liu, N. Chen, D. Deng, X. Xiao and Y. Wang, *Sens. Actuators, B*, 2016, **233**, 615–623.
6 K. Arshak, E. Moore, G. M. Lyons, J. Harris and S. Clifford, *Sens. Rev.*, 2004, **24**(2), 181–198.
7 Z. Fatima, C. R. Gautam, A. Singh, S. K. Avinashi, Shweta, B. C. Yadav and A. A. Khan, *J. Mater. Sci.: Mater. Electron.*, 2022, **33**, 1192–1210.
8 S. Dhall, B. R. Mehta, A. K. Tyagi and K. Sood, *Sensors International*, 2021, **2**, 100116.
9 P. Gouma, K. Kalyanasundaram, X. Yun, M. Stanácevi and L. Wang, *IEEE Sens. J.*, 2010, **10**(1), 49–53.
10 R. Singh, A. K. Yadav and C. R. Gautam, *J. Sens. Technol.*, 2011, **1**(4), 116–124.
11 C. R. Gautam, D. Chakravarty, A. Gautam, C. S. Tiwary, C. F. Woellner, V. K. Mishra, N. Ahmad, S. Ozden, S. Jose, S. Biradar, R. Vajtai, R. Trivedi, D. S. Galvao and P. M. Ajayan, *ACS Omega*, 2018, **3**, 6013–6021.
12 D. Enke, F. Janowski and W. Schwieger, *Microporous Mesoporous Mater.*, 2003, **60**, 19–30.
13 A. Markovi, D. Stoltenberg, D. Enke, E. U. Schlünder and A. Morgenstern, *J. Membr. Sci.*, 2009, **336**, 17–31.
14 T. Tanaka, A. Guilleux, T. Ohyama, Y. Y. Maruo and T. Hayashi, *Sens. Actuators, B*, 1999, **56**, 247–253.
15 L. D. Gelb and K. E. Gubbins, *Langmuir*, 1998, **14**, 2097–2111.
16 L. Du, Y. Li, S. Li, H. Li, L. Li, Y. Cheng and H. Duan, *J. Mater. Sci.: Mater. Electron.*, 2018, **29**, 244–250.
17 L. Song, H. Yue, H. Li, L. Liu, Y. Li, L. Dua, H. Duan and N. I. Klyui, *Chem. Phys. Lett.*, 2018, **699**, 1–7.
18 N. Rajesh, J. C. Kannan, T. Krishnakumar, A. Bonavita, S. G. Leonardi and G. Neri, *Ceram. Int.*, 2015, **41**(10), 14766–14772.
19 K. V. Sopiha, J. H. Kim, S. S. Kim and P. Wu, *Sens. Actuators, B*, 2018, **266**, 344–353.
20 U. Kumar and B. C. Yadav, *J. Taiwan Inst. Chem. Eng.*, 2019, **96**, 652–663.
21 J. Y. Kim, A. Mirzaei, J. H. Kim, J. H. Lee, H. W. Kim and S. S. Kim, *Sens. Actuators, B*, 2019, **296**, 126673.
22 H. M. Ali, E. K. Shokr, Y. A. Taya, S. A. Elkot, M. F. Hasaneen and W. S. Mohamed, *Sens. Actuators, A*, 2022, **335**, 113355.
23 Shweta, P. Dixit, A. Singh, S. K. Avinashi, B. C. Yadav and C. R. Gautam, *J. Non-Cryst. Solids*, 2022, **583**, 121475.
24 M. El-Hezzat, A. Atbir, M. Abid, L. Montagn and F. Méar, *Solid State Sci.*, 2021, **118**, 106666.

25 T. Ishihara, K. Shiokawa, K. Eguchi and H. Arai, *Sens. Actuators*, 1989, **19**, 259–265.

26 Z. Fatima, A. Hussain, C. R. Gautam, Shweta, P. Singh, A. Ahmed, G. Singh and M. K. Singh, *J. Asian Ceram. Soc.*, 2020, **8**, 1108–1126.

27 A. Singh and B. C. Yadav, *Surf. Interfaces*, 2022, **34**, 102368.

28 C. R. Gautam, C. S. Tiwary, S. Jose, G. Brunetto, S. Ozden, S. Vinod, P. Raghavan, S. K. Biradar, D. S. Galvao and P. M. Ajayan, *ACS Nano*, 2015, **22**, 12088–12095.

29 D. E. V. Valerdi, J. A. L. López, J. C. López, G. G. Salgado, A. B. Lara and N. D. E. Torres, *Nanoscale Res. Lett.*, 2014, **9**, 422.

30 I. Asif, S. Ali, S. Shahzadi and S. Mahmood, *J. Chin. Chem. Soc.*, 2007, **54**, 23–30.

31 M. Th. P. Ledent and P. Tarte, *Spectrochim. Acta, Part A*, 1973, **29**, 1007–1016.

32 X. Li, A. Lu and H. Yang, *J. Non-Cryst. Solids*, 2014, **389**, 21–27.

33 M. Uğurlu, *Microporous Mesoporous Mater.*, 2009, **119**, 276–283.

34 W. Wang, H. Li, Y. Guo, Q. Sun and C. Chen, *J. Adv. Ceram.*, 2012, **1**, 283–289.

35 C. R. Gautam and A. K. Yadav, *Opt. Photonics J.*, 2013, **3**, 1–7.

36 M. A. Butturi, M. C. Carotta, G. Martinelli, L. Passari, G. M. Youssef, A. Chiorino and G. Ghiotti, *Solid State Commun.*, 1997, **101**, 11–16.

37 C. R. Gautam, A. K. Yadav and A. K. Singh, *ISRN Ceram.*, 2012, **2012**, 428497.

38 C. Marcolli and G. Calzaferri, *J. Phys. Chem. B*, 1997, **101**, 4925–4933.

39 C. Ivascu, A. T. Gabor, O. Cozar, L. Daraban and I. Ardelean, *J. Mol. Struct.*, 2011, **993**, 249–253.

40 E. V. Jelenkovic, K. Y. Tong, Z. Sun, C. L. Mak and W. Y. Cheung, *J. Vac. Sci. Technol., A*, 1997, **15**, 2836.

41 P. Y. Shih, S. W. Yung and T. S. Chin, *J. Non-Cryst. Solids*, 1998, **224**, 143–152.

42 A. K. Yadav and P. Singh, *RSC Adv.*, 2015, **5**, 67583–67609.

43 C. Wang, G. Deo and I. E. Wachs, *J. Catal.*, 1998, **178**, 640–648.

44 C. Andronache, *Mod. Phys. Lett. B*, 2010, **24**, 2007–2014.

45 C. D. Blasi, C. Branca and A. Galgano, *Polym. Degrad. Stab.*, 2007, **92**, 752–764.

46 X. Wu, R. Su, Y. Zhu and Z. Huang, *RSC Adv.*, 2019, **9**, 4203.

47 Y. Shen, J. C. Jiang, P. Zeman, V. Šímová, J. Vlček and E. I. Meletis, *Sci. Rep.*, 2019, **9**, 3603.

48 J. Paillier, C. Mickel, P. F. Gostin and A. Gebert, *Mater. Charact.*, 2010, **61**, 1000–1008.

49 M. Naderi, *Progress in Filtration and Separation*, Academic Press, 2015, pp. 585–608.

50 C. Sriwong, C. Phrompet, W. Tuichai, A. Karaphun, K. Kurosaki and C. Ruttanapun, *Sci. Rep.*, 2020, **10**, 11077.

51 S. Kwon, H. Hwang and Y. Lee, *Crystals*, 2019, **9**(10), 528.

52 A. Singh, S. Sikarwar and B. C. Yadav, *Mater. Res. Express*, 2021, **8**, 045013.

53 H. Zhang, J. Feng, L. Li, Y. Jiang and J. Feng, *RSC Adv.*, 2019, **9**, 5967.

54 J. Herrán, G. G. Mandayo, I. Ayerdi and E. Castãno, *Sens. Actuators, B*, 2008, **129**, 386–390.

55 A. Patil, C. Dighavkar and R. Borse, *J. Optoelectron.*, 2011, **13**, 1331–1337.

56 Y. Wang, K. Zhang, J. Zou, X. Wang, L. Sun, T. Wang and Q. Zhang, *Carbon*, 2017, **117**, 263–270.

57 Y. Chen, D. Wang, H. Qin, H. Zhang, Z. Zhang, G. Zhou, C. Gao and J. Hu, *J. Rare Earths*, 2019, **37**, 80–87.